10

Creation of Ordered Layers on Semiconductor Surfaces: An ab Initio Molecular Dynamics Study of the SiC(001)-3×2 and SiC(100)-c(2×2) Surfaces

Yanli Zhang and Mark E. Tuckerman
Department of Chemistry, New York University
USA

1. Introduction

The chemistry of hybrid structures composed of organic molecules and semiconductor surfaces is opening up exciting new areas of development in molecular electronics, nanoscale sensing devices, and surface lithography (Filler & Bent, 2002; Kachian et al., 2010; Kruse & Wolkow, 2002). Covalent attachment of organic molecules to a semiconducting surface can yield active devices, such as molecular switches (Filler & Bent, 2003; Flatt et al., 2005; Guisinger, Basu, Greene, Baluch & Hersam, 2004; Guisinger, Greene, Basu, Baluch & Hersam, 2004; He et al., 2006; Rakshit et al., 2004) and sensors (Cattaruzza et al., 2006) or passivating insulating layers. Moreover, it is assumed that the reactions can be controlled by "engineering" specific modifications to organic molecules, suggesting possible new lithographic techniques.

One of the goals of controlling the surface chemistry is the creation of ordered nanostructures on semiconducting surfaces. Indeed, there has been some success in obtaining locally ordered structures on the hydrogen terminated Si(100) surface (Basu et al., 2006; Hossain et al., 2005b; Kirczenow et al., 2005; Lopinski et al., 2000; Pitters et al., 2006). These methods require a dangling Si bond without a hydrogen to initialize the self-replicating reaction. Another popular approach eliminates the initialization step by exploiting the reactivity between surface dimers on certain reconstructed surfaces with the π bonds in many organic molecules. The challenge with this approach lies in designing the surface and/or the molecule so as to eliminate all but one desired reaction channel. Charge asymmetries, such as occur on the Si(100)-2×1 surface, lead to a violation of the usual Woodward-Hoffman selection rules, which govern many purely organic reactions, allowing a variety of possible [4+2] and [2+2] surface adducts.

Silicon-carbide (SiC) is often the material of choice for electronic and sensor applications under extreme conditions (Capano & Trew, 1997; Mélinon et al., 2007; Starke, 2004) or subject to biocompatibility constraints (Stutzmann et al., 2006). SiC has a variety of reconstructions that could possibly serve as candidates for creating ordered organic/semiconductor interfaces. However, the choice of the reconstruction is crucial. Multiple reactive sites, such as occur on some of the SiC surfaces, will lead to a broad distribution of adducts.

The exploration of hybrid organic-semiconductor materials and the reactions associated with them is an area in which theoretical and computational tools can play an important role. Indeed, modern theoretical methods combined with high-performance computing,

have advanced to a level such that the thermodynamics and reaction mechanisms can be routinely studied. These studies can aid in the interpretation of experimental results and can leverage theoretical mechanisms to predict the outcomes of new experiments. This chapter will focus on a description of one set of such techniques, namely, those based on density functional theory and first-principles or *ab initio* molecular dynamics (Car & Parrinello, 1985; Marx & Hutter, 2000; 2009; Tuckerman, 2002). As these methods employ an explicit representation of the electronic structure, electron localization techniques can be used to follow local electronic rearrangements during a reaction and, therefore, generate a clear picture of the reaction mechanism. In addition, statistical mechanical tools can be employed to obtain thermodynamic properties of the reaction products, including relative free energies and populations of the various products. Following a detailed description of the computational approaches, we will present two applications of conjugated dienes reacting with different choices of SiC surfaces (Hayes & Tuckerman, 2008). We will investigate how the surface structure influences the thermodynamics of the reaction products and how these thermodynamic properties can be used to guide the choice of the surface in order to control the product distribution and associated free energies.

2. Computational methods

Because the problem of covalently attaching an organic molecule to a semiconductor surface requires the formation of chemical bonds, a theoretical treatment of this problem must be able to describe this bond formation process, which generally requires an *ab initio* approach in which the electronic structure is accounted for explicitly. Assuming the validity of the Born-Oppenheimer approximation, the goal of any *ab initio* approach is to approximate the ground-state solution of the electronic Schrödinger equation $\hat{H}_{\text{elec}}(\mathbf{R})|\Psi_0(\mathbf{R})\rangle = E_0(\mathbf{R})|\Psi_0(\mathbf{R})\rangle$, where $\hat{H}_{\text{elec}}$ is the electronic Hamiltonian, and $\mathbf{R}$ denotes a classical configuration of the chemical nuclei in the system. Ultimately, in order to predict reaction mechanisms and thermodynamics, one needs to use the approximate solution of the Schrödinger equation to propagate the nuclei dynamically using Newton's laws of motion. This is the essence of the method known as *ab initio* molecular dynamics (AIMD) (Car & Parrinello, 1985; Marx & Hutter, 2000; 2009; Tuckerman, 2002). Unless otherwise stated, all of the calculations to be presented in this chapter were carried out using the implementation of plane-wave based AIMD implemented in the PINY_MD package (Tuckerman et al., 2000).

In this section, we will briefly review density functional theory (DFT) as the electronic structure method of choice for the studies to be described in this chapter. DFT represents an optimal compromise between accuracy and computational efficiency. This is an important consideration, as a typical AIMD calculation requires that the electronic structure problem be solved tens to hundreds of thousands of time in order to generate one or more trajectories of sufficient length to extract dynamic and thermodynamic properties. We will then describe the AIMD approach, including several technical considerations such as basis sets, boundary conditions, and electron localization schemes.

2.1 Density functional theory

As noted above, we seek approximate solutions to the electronic Schrödinger equation. To this end, we begin by considering a system of N nuclei at positions $\mathbf{R}_1, ..., \mathbf{R}_N \equiv \mathbf{R}$ and M electrons with coordinate labels $\mathbf{r}_1, ..., \mathbf{r}_M$ and spin states $s_1, ..., s_M$. The fixed nuclear positions

allow us to define the electronic Hamiltonian (in atomic units) as

$$\hat{H}_{\text{elec}}(\mathbf{R}) = -\frac{1}{2}\sum_{i=1}^{M}\nabla_i^2 + \sum_{i>j}\frac{1}{|\mathbf{r}_i - \mathbf{r}_j|} - \sum_{I=1}^{N}\sum_{i=1}^{M}\frac{Z_I}{|\mathbf{R}_I - \mathbf{r}_i|} \tag{1}$$

where Z_I is the charge on the Ith nucleus. The time-independent electronic Schrödinger equation or electronic eigenvalue problem

$$\left[-\frac{1}{2}\sum_{i=1}^{M}\nabla_i^2 + \sum_{i>j}\frac{1}{|\mathbf{r}_i - \mathbf{r}_j|} - \sum_{I=1}^{N}\sum_{i=1}^{M}\frac{Z_I}{|\mathbf{R}_I - \mathbf{r}_i|}\right]\Psi(\mathbf{x}_1,...,\mathbf{x}_M,\mathbf{R}) = E(\mathbf{R})\Psi(\mathbf{x}_1,...,\mathbf{x}_M,\mathbf{R}) \tag{2}$$

which assumes the validity of the Born-Oppenheimer approximation, could, in principle, yield all of the electronic energy levels and eigenfunctions at the given nuclear configuration $\mathbf{R}$. Here $\mathbf{x}_i = \mathbf{r}_i, s_i$ is a combination of coordinate and spin variables. Unfortunately, for large condensed-phase problems of the type to be considered here, an exact solution of the electronic eigenvalue problem is computationally intractable.

The Kohn-Sham (KS) (Kohn & Sham, 1965) formulation of density functional theory (DFT) (Hohenberg & Kohn, 1964) replaces the fully interacting electronic system described by Eq. (2) by an equivalent non-interacting system that is required to yield the same *ground-state* energy and wave function as the original interacting system. As the name implies, the central quantity in DFT is the ground-state density $n_0(\mathbf{r})$ generated from the ground-state wave function Ψ_0 via

$$n_0(\mathbf{r}) = M\sum_{s_1=-1/2}^{1/2}\cdots\sum_{s_M=-1/2}^{1/2}\int d\mathbf{r}_2\cdot d\mathbf{r}_M|\Psi_0(\mathbf{r},s_1,...,\mathbf{x}_M)|^2 \tag{3}$$

where, for notational convenience, the dependence on $\mathbf{R}$ is left off. The central theorem of DFT is the Hohenberg-Kohn theorem, which states that there exists an exact energy $E[n]$ that is a functional of electronic densities $n(\mathbf{r})$ such that when $E[n]$ is minimized with respect to $n(\mathbf{r})$ subject to the constraint that $\int d\mathbf{r}\ n(\mathbf{r}) = M$ (each $n(\mathbf{r})$ must yield the correct number of electrons), the true ground-state density $n_0(\mathbf{r})$ is obtained. The true ground-state energy is then given by $E_0 = E[n_0]$. The KS noninteracting system is constructed in terms of a set of mutually orthogonal single-particle orbitals $\psi_i(\mathbf{r})$ in terms of which the density $n(\mathbf{r})$ is given by

$$n(\mathbf{r}) = \sum_{i=1}^{N_s} f_i|\psi_i(\mathbf{r})|^2 \tag{4}$$

where f_i are the occupation numbers of a set of N_s such orbitals, where $\sum_i f_i = M$. In closed-shell systems, the orbitals are all doubly occupied so that $N_s = M/2$, and $f_i = 2$. In open-shell systems, we treat all of the electrons in double and singly occupied orbitals explicitly and take $N_s = M$. When virtual or unoccupied orbitals are needed, we can take $N_s > M/2$ or $N_s > M$ for closed and open-shell systems, respectively, and take $f_i = 0$ for the virtual orbitals.

In KS theory, the energy functional is taken to be

$$\mathcal{E}[\{\psi\}] = -\frac{1}{2}\sum_{i=1}^{N_s} f_i\langle\psi_i|\nabla^2|\psi_i\rangle + \frac{1}{2}\int d\mathbf{r}\ d\mathbf{r}'\ \frac{n(\mathbf{r})n(\mathbf{r}')}{|\mathbf{r}-\mathbf{r}'|} + E_{\text{xc}}[n] + \int d\mathbf{r}\ n(\mathbf{r})V_{\text{ext}}(\mathbf{r},\mathbf{R}) \tag{5}$$

The first term in the functional represents the noninteracting quantum kinetic energy of the electrons, the second term is the direct Coulomb interaction between two charge distributions, the third therm is the exchange-correlation energy, whose exact form is unknown, and the fourth represents the "external" Coulomb potential on the electrons due to the fixed nuclei, $V_{\text{ext}}(\mathbf{r},\mathbf{R}) = -\sum_I Z_I/|\mathbf{r}-\mathbf{R}_I|$. Minimization of Eq. (5) with respect to the orbitals subject to the orthogonality constraint leads to a set of coupled self-consistent field equations of the form

$$\left[-\frac{1}{2}\nabla^2 + V_{\text{KS}}(\mathbf{r})\right]\psi_i(\mathbf{r}) = \sum_j \lambda_{ij}\psi_j(\mathbf{r}) \tag{6}$$

where the KS potential $V_{\text{KS}}(\mathbf{r})$ is given by

$$V_{\text{KS}}(\mathbf{r}) = \int d\mathbf{r}' \, \frac{n(\mathbf{r}')}{|\mathbf{r}-\mathbf{r}'|} + \frac{\delta E_{\text{xc}}}{\delta n(\mathbf{r})} + V_{\text{ext}}(\mathbf{r},\mathbf{R}) \tag{7}$$

and λ_{ij} is a set of Lagrange multipliers used to enforce the orthogonality constraint $\langle\psi_i|\psi_j\rangle = \delta_{ij}$. If we introduce a unitary transformation U that diagonalizes the matrix λ_{ij} into Eq. (6), then we obtain the Kohn-Sham equations in the form

$$\left[-\frac{1}{2}\nabla^2 + V_{\text{KS}}(\mathbf{r})\right]\phi_i(\mathbf{r}) = \varepsilon_i\phi_i(\mathbf{r}) \tag{8}$$

where $\phi_i(\mathbf{r}) = \sum_j U_{ij}\psi_j(\mathbf{r})$ are the KS orbitals and ε_i are the KS energy levels, i.e., the eigenvalues of the matrix λ_{ij}. If the exact exchange-correlation functional were known, the KS theory would be exact. However, because $E_{\text{xc}}[n]$ is unknown, approximations must be introduced for this term in practice. The accuracy of DFT results depends critically on the quality of the approximation. One of the most widely used forms for $E_{\text{xc}}[n]$ is known as the generalized-gradient approximation (GGA), where in $E_{\text{xc}}[n]$ is approximated as a local functional of the form

$$E_{\text{xc}}[n] \approx \int d\mathbf{r} \, f_{\text{GGA}}(n(\mathbf{r}), |\nabla n(\mathbf{r})|) \tag{9}$$

where the form of the function f_{GGA} determines the specific GGA approximation. Commonly used GGA functionals are the Becke-Lee-Yang-Parr (BLYP) (1988; 1988) and Perdew-Burke-Ernzerhof (PBE) (1996) functionals.

2.2 Ab initio molecular dynamics

Solution of the KS equations yields the electronic structure at a set of fixed nuclear positions $\mathbf{R}_1, ..., \mathbf{R}_N \equiv \mathbf{R}$. Thus, in order to follow the progress of a chemical reaction, we need an approach that allows us to propagate the nuclei in time. If we assume the nuclei can be treated as classical point particles, then we seek the nuclear positions $\mathbf{R}_1(t), ..., \mathbf{R}_N(t)$ as functions of time, which are given by Newton's second law

$$M_I\ddot{\mathbf{R}}_I = \mathbf{F}_I \tag{10}$$

where M_I and $\mathbf{F}_I$ are the mass and total force on the Ith nucleus. If the exact ground-state wave function $\Psi_0(\mathbf{R})$ were known, then the forces would be given by the Hellman-Feynman theorem

$$\mathbf{F}_I = -\langle\Psi_0(\mathbf{R})|\nabla_I\hat{H}_{\text{elec}}(\mathbf{R})|\Psi_0(\mathbf{R})\rangle - \nabla_I U_{\text{NN}}(\mathbf{R}) \tag{11}$$

where we have introduced the nuclear-nuclear Coulomb repulsion

$$U_{\mathrm{NN}}(\mathbf{R}) = \sum_{I>J} \frac{Z_I Z_J}{|\mathbf{R}_I - \mathbf{R}_J|} \tag{12}$$

Within the framework of KS DFT, the force expression becomes

$$\mathbf{F}_I = -\int d\mathbf{r}\; n_0(\mathbf{r}) \nabla_I V_{\mathrm{ext}}(\mathbf{r}, \mathbf{R}) - \nabla_I U_{\mathrm{NN}}(\mathbf{R}) \tag{13}$$

The equations of motion, Eq. (10), are integrated numerically for a set of discrete times $t = 0, \Delta t, 2\Delta t, ..., \mathcal{N}\Delta t$ subject to a set of initial coordinates $\mathbf{R}_1(0), ..., \mathbf{R}_N(0)$ and velocities $\dot{\mathbf{R}}_1(0), ..., \dot{\mathbf{R}}_N(0)$ using a solver such as the velocity Verlet algorithm:

$$\begin{aligned} \mathbf{R}_I(\Delta t) &= \mathbf{R}_I(0) + \Delta t \dot{\mathbf{R}}_I(0) + \frac{\Delta t^2}{2M_I}\mathbf{F}_I(0) \\ \dot{\mathbf{R}}_I(\Delta t) &= \dot{\mathbf{R}}_I(0) + \frac{\Delta t}{2M_I}\left[\mathbf{F}_I(0) + \mathbf{F}_I(\Delta t)\right] \end{aligned} \tag{14}$$

where $\mathbf{F}_I(0)$ and $\mathbf{F}_I(\Delta t)$ are the forces at $t = 0$ and $t = \Delta t$, respectively. Iteration of Eq. (14) yields a full trajectory of $\mathcal{N}$ steps. Eqs. (13) and (14) suggest an algorithm for generating the finite-temperature dynamics of a system using forces generated from electronic structure calculations performed "on the fly" as the simulation proceeds: Starting with the initial nuclear configuration, one minimizes the KS energy functional to obtain the ground-state density, and Eq. (13) is used to obtain the initial forces. These forces are then used to propagate the nuclear positions to the next time step using the first of Eqs. (14). At this new nuclear configuration, the KS functional is minimized again to obtain the new ground-state density and forces using Eq. (13), and these forces are used to propagate the velocities to time $t = \Delta t$. These forces can also be used again to propagate the positions to time $t = 2\Delta t$. The procedure is iterated until a full trajectory is generated. This approach is known as "Born-Oppenheimer" dynamics because it employs, at each step, an electronic configuration that is fully quenched to the ground-state Born-Oppenheimer surface.

An alternative to Born-Oppenheimer dynamics is the Car-Parrinello (CP) method (Car & Parrinello, 1985; Marx & Hutter, 2000; Tuckerman, 2002). In this approach, an initially minimized electronic configuration is subsequently "propagated" from one nuclear configuration to the next using a fictitious Newtonian dynamics for the orbitals. In this "dynamics", the orbitals are given a small amount of thermal kinetic energy and are made "light" compared to the nuclei. Under these conditions, the orbitals actually generate a potential of mean force surface that is very close to the true Born-Oppenheimer surface. The equations of motion of the CP method are

$$\begin{aligned} M_I \ddot{\mathbf{R}}_I &= -\nabla_I \left[\mathcal{E}[\{\psi\}, \mathbf{R}] + U_{\mathrm{NN}}(\mathbf{R})\right] \\ \mu|\ddot{\psi}_i\rangle &= -\frac{\partial}{\partial\langle\psi_i|}\mathcal{E}[\{\psi\}, \mathbf{R}] + \sum_j \lambda_{ij}|\psi_j\rangle \end{aligned} \tag{15}$$

where μ is a mass-like parameter for the orbitals (which actually has units of energy$\times$ time^2), and λ_{ij} is the Lagrange multiplier matrix that enforces the orthogonality of the orbitals as a holonomic constraint on the fictitious orbital dynamics. Choosing μ small ensures that the

orbital dynamics is adiabatically decoupled from the true nuclear dynamics, thereby allowing the orbitals to generate the aforementioned potential of mean force surface. For a detailed analysis of the CP dynamics, see Marx et al. (1999); Tuckerman (2002). As an illustration of the CP dynamics, Fig. 1 of Tuckerman & Parrinello (1994) shows the temperature profile for a short CPAIMD simulation of bulk silicon together with the kinetic energy profile from the fictitious orbital dynamics. The figure demonstrates that the orbital dynamics is essentially a "slave" to the nuclear dynamics, which shows that the electronic configuration closely follows that dynamics of the nuclei in the spirit of the Born-Oppenheimer approximation.

2.3 Plane wave basis sets and surface boundary conditions

In AIMD calculations, the most commonly employed boundary conditions are periodic boundary conditions, in which the system is replicated infinitely in all three spatial directions. This is clearly a natural choice for solids and is particularly convenient for liquids. In an infinite periodic system, the KS orbitals become Bloch functions of the form

$$\psi_{i\mathbf{k}}(\mathbf{r}) = e^{i\mathbf{k}\cdot\mathbf{r}} u_{i\mathbf{k}}(\mathbf{r}) \tag{16}$$

where $\mathbf{k}$ is a vector in the first Brioullin zone and $u_{i\mathbf{k}}(\mathbf{r})$ is a periodic function. A natural basis set for expanding a periodic function is the Fourier or plane wave basis set, in which $u_{i\mathbf{k}}(\mathbf{r})$ is expanded according to

$$u_{i\mathbf{k}}(\mathbf{r}) = \frac{1}{\sqrt{V}} \sum_{\mathbf{g}} c_{i,\mathbf{g}}^{\mathbf{k}} e^{i\mathbf{g}\cdot\mathbf{r}} \tag{17}$$

where V is the volume of the cell, $\mathbf{g} = 2\pi\mathbf{h}^{-1}\hat{\mathbf{g}}$ is a reciprocal lattice vector, $\mathbf{h}$ is the cell matrix, whose columns are the cell vectors ($V = \det(\mathbf{h})$), $\hat{\mathbf{g}}$ is a vector of integers, and $\{c_{i,\mathbf{g}}^{\mathbf{k}}\}$ are the expansion coefficients. An advantage of plane waves is that the sums needed to go back and forth between reciprocal space and real space can be performed efficiently using fast Fourier transforms (FFTs). In general, the properties of a periodic system are only correctly described if a sufficient number of $\mathbf{k}$-vectors are sampled from the Brioullin zone. However, for the applications we will consider, we are able to choose sufficiently large system sizes that we can restrict our $\mathbf{k}$-point sampling to the single point, $\mathbf{k} = (0, 0, 0)$, known as the Γ-point. At the Γ-point, the plane wave expansion reduces to

$$\psi_i(\mathbf{r}) = \frac{1}{\sqrt{V}} \sum_{\mathbf{g}} c_{i,\mathbf{g}} e^{i\mathbf{g}\cdot\mathbf{r}} \tag{18}$$

At the Γ-point, the orbitals can always be chosen to be real functions. Therefore, the plane-wave expansion coefficients satisfy the property that $c_{i,\mathbf{g}}^{*} = c_{i,-\mathbf{g}}$, which requires keeping only half of the full set of plane-wave expansion coefficients. In actual applications, plane waves up to a given cutoff $|\mathbf{g}|^2/2 < E_{\text{cut}}$ are retained. Similarly, the density $n(\mathbf{r})$ given by Eq. (4) can also be expanded in a plane wave basis:

$$n(\mathbf{r}) = \frac{1}{V} \sum_{\mathbf{g}} n_{\mathbf{g}} e^{i\mathbf{g}\cdot\mathbf{r}} \tag{19}$$

However, since $n(\mathbf{r})$ is obtained as a square of the KS orbitals, the cutoff needed for this expansion is $4E_{\text{cut}}$ for consistency with the orbital expansion.

At first glance, it might seem that plane waves are ill-suited to treat surfaces because of their two-dimensional periodicity. However, in a series of papers (Minary et al., 2004; 2002;

Tuckerman & Martyna, 1999), Martyna, Tuckerman, and coworkers showed that clusters (systems with no periodicity), wires (systems with one periodic dimension), and surfaces (systems with two periodic dimensions) could all be treated using a plane-wave basis within a single unified formalism. Let $n(\mathbf{r})$ be a particle density with a Fourier expansion given by Eq. (19), and let $\phi(\mathbf{r}-\mathbf{r}')$ denote an interaction potential. In a fully periodic system, the energy of a system described by $n(\mathbf{r})$ and $\phi(\mathbf{r}-\mathbf{r}')$ is given by

$$E = \frac{1}{2}\int d\mathbf{r}\, d\mathbf{r}'\; n(\mathbf{r})\phi(\mathbf{r}-\mathbf{r}')n(\mathbf{r}') = \frac{1}{2V}\sum_{\mathbf{g}} |n_{\mathbf{g}}|^2 \tilde{\phi}_{-\mathbf{g}} \tag{20}$$

where $\tilde{\phi}_{\mathbf{g}}$ is the Fourier transform of the potential. For systems with fewer than three periodic dimensions, the idea is to replace Eq. (20) with its first-image approximation

$$E \approx E^{(1)} \equiv \frac{1}{2V}\sum_{\mathbf{g}} |n_{\mathbf{g}}|^2 \bar{\phi}_{-\mathbf{g}} \tag{21}$$

where $\bar{\phi}_{\mathbf{g}}$ denotes a Fourier expansion coefficient of the potential in the non-periodic dimensions and a Fourier transform along the periodic dimensions. For clusters, $\bar{\phi}_{\mathbf{g}}$ is given by

$$\bar{\phi}_{\mathbf{g}} = \int_{-L_z/2}^{L_z/2} dz \int_{-L_y/2}^{L_y/2} dy \int_{-L_x/2}^{L_x/2} dx\; \phi(\mathbf{r}) e^{-i\mathbf{g}\cdot\mathbf{r}} \tag{22}$$

for wires, it becomes

$$\bar{\phi}_{\mathbf{g}} = \int_{-L_z/2}^{L_z/2} dz \int_{-L_y/2}^{L_y/2} dy \int_{-\infty}^{\infty} dx\; \phi(\mathbf{r}) e^{-i\mathbf{g}\cdot\mathbf{r}} \tag{23}$$

and for surfaces, we obtain

$$\bar{\phi}_{\mathbf{g}} = \int_{-L_z/2}^{L_z/2} dz \int_{-\infty}^{\infty} dy \int_{-\infty}^{\infty} dx\; \phi(\mathbf{r}) e^{-i\mathbf{g}\cdot\mathbf{r}} \tag{24}$$

The error in the first-image approximation drops off as a function of the volume, area, or length in the non-periodic directions, as analyzed in Minary et al. (2004; 2002); Tuckerman & Martyna (1999).
In order to have an expression that is easily computed within the plane wave description, consider two functions $\phi^{\text{long}}(\mathbf{r})$ and $\phi^{\text{short}}(\mathbf{r})$, which are assumed to be the long and short range contributions to the total potential, i.e.

$$\phi(\mathbf{r}) = \phi^{\text{long}}(\mathbf{r}) + \phi^{\text{short}}(\mathbf{r})$$

$$\bar{\phi}(\mathbf{g}) = \bar{\phi}^{\text{long}}(\mathbf{g}) + \bar{\phi}^{\text{short}}(\mathbf{g}). \tag{25}$$

We require that $\phi^{\text{short}}(\mathbf{r})$ vanish exponentially quickly at large distances from the center of the parallelepiped and that $\phi^{\text{long}}(\mathbf{r})$ contain the long range dependence of the full potential, $\phi(\mathbf{r})$.

With these two requirements, it is possible to write

$$\begin{aligned}\bar{\phi}^{\text{short}}(\mathbf{g}) &= \int_{D(V)} d\mathbf{r}\, e^{-i\mathbf{g}\cdot\mathbf{r}}\phi^{\text{short}}(\mathbf{r}) \\ &= \int_{\text{all space}} d\mathbf{r} e^{-i\mathbf{g}\cdot\mathbf{r}}\phi^{\text{short}}(\mathbf{r}) + \epsilon(\mathbf{g}) \\ &= \tilde{\phi}^{\text{short}}(\mathbf{g}) + \epsilon(\mathbf{g}) \end{aligned} \tag{26}$$

with exponentially small error, $\epsilon(\mathbf{g})$, provided the range of $\phi^{\text{short}}(\mathbf{r})$ is small compared size of the parallelepiped. In order to ensure that Eq. (26) is satisfied, a convergence parameter, α, is introduced which can be used to adjust the range of $\phi^{\text{short}}(\mathbf{r})$ such that $\epsilon(\mathbf{g}) \sim 0$ and the error, $\epsilon(\mathbf{g})$, will be neglected in the following.
The function, $\tilde{\phi}^{\text{short}}(\mathbf{g})$, is the Fourier transform of $\phi^{\text{short}}(\mathbf{r})$. Therefore,

$$\begin{aligned}\bar{\phi}(\mathbf{g}) &= \bar{\phi}^{\text{long}}(\mathbf{g}) + \tilde{\phi}^{\text{short}}(\mathbf{g}) \\ &= \bar{\phi}^{\text{long}}(\mathbf{g}) - \tilde{\phi}^{\text{long}}(\mathbf{g}) + \tilde{\phi}^{\text{short}}(\mathbf{g}) + \tilde{\phi}^{\text{long}}(\mathbf{g}) \\ &= \hat{\phi}^{\text{screen}}(\mathbf{g}) + \tilde{\phi}(\mathbf{g}) \end{aligned} \tag{27}$$

where $\tilde{\phi}(\mathbf{g}) = \tilde{\phi}^{\text{short}}(\mathbf{g}) + \tilde{\phi}^{\text{long}}(\mathbf{g})$ is the Fourier transform of the full potential, $\phi(\mathbf{r}) = \phi^{\text{short}}(\mathbf{r}) + \phi^{\text{long}}(\mathbf{r})$ and

$$\hat{\phi}^{\text{screen}}(\mathbf{g}) = \bar{\phi}^{\text{long}}(\mathbf{g}) - \tilde{\phi}^{\text{long}}(\mathbf{g}). \tag{28}$$

Thus, Eq. (28) becomes leads to

$$\langle\phi\rangle = \frac{1}{2V}\sum_{\hat{\mathbf{g}}} |\bar{n}(\mathbf{g})|^2 \left[\tilde{\phi}(-\mathbf{g}) + \hat{\phi}^{\text{screen}}(-\mathbf{g})\right] \tag{29}$$

The new function appearing in the average potential energy, Eq. (29), is the difference between the Fourier series and Fourier transform form of the long range part of the potential energy and will be referred to as the screening function because it is constructed to "screen" the interaction of the system with an infinite array of periodic images. The specific case of the Coulomb potential, $\phi(\mathbf{r}) = 1/r$, can be separated into short and long range components via

$$\frac{1}{r} = \frac{\text{erf}(\alpha r)}{r} + \frac{\text{erfc}(\alpha r)}{r} \tag{30}$$

where the first term is long range. The parameter α determines the specific ranges of these terms. The screening function for the cluster case is easily computed by introducing an FFT grid and performing the integration numerically (Tuckerman & Martyna, 1999). For the wire (Minary et al., 2002) and surface (Minary et al., 2004) cases, analytical expressions can be

worked out. In particular, for surfaces, the screening function is

$$\begin{aligned}\bar{\phi}^{\text{screen}}(\mathbf{g}) = -\frac{4\pi}{g^2}\Bigg\{&\cos\left(\frac{g_c L_c}{2}\right) \\ &\times \left[\exp\left(-\frac{g_s L_c}{2}\right) - \frac{1}{2}\exp\left(-\frac{g_s L_c}{2}\right)\operatorname{erfc}\left(\frac{\alpha^2 L_c - g_s}{2\alpha}\right)\right. \\ &\left. - \frac{1}{2}\exp\left(\frac{g_s L_c}{2}\right)\operatorname{erfc}\left(\frac{\alpha^2 L_c + g_s}{2\alpha}\right)\right] \\ &+ \exp\left(-\frac{g^2}{4\alpha^2}\right)\operatorname{Re}\left[\operatorname{erfc}\left(\frac{\alpha^2 L_c + i g_c}{2\alpha}\right)\right]\Bigg\}\end{aligned} \tag{31}$$

When a plane wave basis set is employed, the external energy is made somewhat complicated by the fact that very large basis sets are needed to treat the rapid spatial fluctuations of core electrons. Therefore, core electrons are often replaced by atomic pseudopotentials or augmented plane wave techniques. Here, we shall discuss the former. In the atomic pseudopotential scheme, the nucleus plus the core electrons are treated in a frozen core type approximation as an "ion" carrying only the valence charge. In order to make this approximation, the valence orbitals, which, in principle must be orthogonal to the core orbitals, must see a different pseudopotential for each angular momentum component in the core, which means that the pseudopotential must generally be nonlocal. In order to see this, we consider a potential operator of the form

$$\hat{V}_{\text{pseud}} = \sum_{l=0}^{\infty}\sum_{m=-l}^{l} v_l(r)|lm\rangle\langle lm| \tag{32}$$

where r is the distance from the ion, and $|lm\rangle\langle lm|$ is a projection operator onto each angular momentum component. In order to truncate the infinite sum over l in Eq. (32), we assume that for some $l \geq \bar{l}$, $v_l(r) = v_{\bar{l}}(r)$ and add and subtract the function $v_{\bar{l}}(r)$ in Eq. (32):

$$\begin{aligned}\hat{V}_{\text{pseud}} &= \sum_{l=0}^{\infty}\sum_{m=-l}^{l}(v_l(r) - v_{\bar{l}}(r))|lm\rangle\langle lm| + v_{\bar{l}}(r)\sum_{l=0}^{\infty}\sum_{m=-l}^{l}|lm\rangle\langle lm| \\ &= \sum_{l=0}^{\infty}\sum_{m=-l}^{l}(v_l(r) - v_{\bar{l}}(r))|lm\rangle\langle lm| + v_{\bar{l}}(r) \\ &\approx \sum_{l=0}^{\bar{l}-1}\sum_{m=-l}^{l}\Delta v_l(r)|lm\rangle\langle lm| + v_{\bar{l}}(r)\end{aligned} \tag{33}$$

where the second line follows from the fact that the sum of the projection operators is unity, $\Delta v_l(r) = v_l(r) - v_{\bar{l}}(r)$, and the sum in the third line is truncated before $\Delta v_l(r) = 0$. The complete pseudopotential operator is

$$\hat{V}_{\text{pseud}}(r; \mathbf{R}_1, ..., \mathbf{R}_N) = \sum_{I=1}^{N}\left[v_{\text{loc}}(|\mathbf{r} - \mathbf{R}_I|) + \sum_{l=0}^{\bar{l}-1}\Delta v_l(|\mathbf{r} - \mathbf{R}_I|)|lm\rangle\langle lm|\right] \tag{34}$$

where $v_{\rm loc}(r) \equiv v_I(r)$ is known as the local part of the pseudopotential (having no projection operator attached to it). Now, the external energy, being derived from the ground-state expectation value of a one-body operator, is given by

$$\varepsilon_{\rm ext} = \sum_i f_i \langle \psi_i | \hat{V}_{\rm pseud} | \psi_i \rangle \tag{35}$$

The first (local) term gives simply a local energy of the form

$$\varepsilon_{\rm loc} = \sum_{I=1}^{N} \int d\mathbf{r}\; n(\mathbf{r}) v_{\rm loc}(|\mathbf{r} - \mathbf{R}_I|) \tag{36}$$

which can be evaluated in reciprocal space as

$$\varepsilon_{\rm loc} = \frac{1}{\Omega} \sum_{I=1}^{N} \sum_{\mathbf{g}} n^*_{\mathbf{g}} \tilde{v}_{\rm loc}(\mathbf{g}) e^{-i\mathbf{g}\cdot\mathbf{R}_I} \tag{37}$$

where $\tilde{V}_{\rm loc}(\mathbf{g})$ is the Fourier transform of the local potential. Note that at $\mathbf{g} = (0,0,0)$, only the nonsingular part of $\tilde{v}_{\rm loc}(\mathbf{g})$ contributes. In the evaluation of the local term, it is often convenient to add and subtract a long-range term of the form $Z_I {\rm erf}(\alpha_I r)/r$, where ${\rm erf}(x)$ is the error function, each ion in order to obtain the nonsingular part explicitly and a residual short-range function $\bar{v}_{\rm loc}(|\mathbf{r} - \mathbf{R}_I|) = v_{\rm loc}(|\mathbf{r} - \mathbf{R}_I|) - Z_I {\rm erf}(\alpha_I |\mathbf{r} - \mathbf{R}_I|)/|\mathbf{r} - \mathbf{R}_I|$ for each ionic core.

2.4 Electron localization methods

An important feature of the KS energy functional is the fact that the total energy $E[\{\psi\}, \mathbf{R}]$ is invariant with respect to a unitary transformation within space of occupied orbitals. That is, if we introduce a new set of orbitals $\psi'_i(\mathbf{r})$ related to the $\psi_i(\mathbf{r})$ by

$$\psi'_i(\mathbf{r}) = \sum_{j=1}^{N_{\rm s}} U_{ij} \psi_j(\mathbf{r}) \tag{38}$$

where U_{ij} is a $N_{\rm s} \times N_{\rm s}$ unitary matrix, the energy $E[\{\psi'\}, \mathbf{R}] = E[\{\psi\}, \mathbf{R}]$. We say that the energy is invariant with respect to the group SU($N_{\rm s}$), i.e., the group of all $N_{\rm s} \times N_{\rm s}$ unitary matrices with unit determinant. This invariance is a type of gauge invariance, specifically that in the occupied orbital subspace. The fictitious orbital dynamics of the AIMD scheme as written in Eqs. (15) does not preserve any particular unitary representation or gauge of the orbitals but allows the orbitals to mix arbitrarily according to Eq. (38). This mixing happens intrinsically as part of the dynamics rather than by explicit application of the unitary transformation.

Although this arbitrariness has no effect on the nuclear dynamics, it is often desirable for the orbitals to be in a particular unitary representation. For example, we might wish to have the true Kohn-Sham orbitals at each step in an AIMD simulation in order to calculate the Kohn-Sham eigenvalues and generate the corresponding density of states from a histogram of these eigenvalues. This would require choosing U_{ij} to be the unitary transformation that diagonalizes the matrix of Lagrange multipliers in Eq. (6). Another important representation is that in which the orbitals are maximally localized in real space. In this representation, the orbitals are closest to the classic "textbook" molecular orbital picture.

In order to obtain the unitary transformation U_{ij} that generates maximally localized orbitals, we seek a functional that measures the total spatial spread of the orbitals. One possibility for this functional is simply to use the variance of the position operator $\hat{\mathbf{r}}$ with respect to each orbital and sum these variances:

$$\Omega[\{\psi\}] = \sum_{i=1}^{N_s} \left[\langle \psi_i | \hat{r}^2 | \psi_i \rangle - \langle \psi_i | \hat{\mathbf{r}} | \psi_i \rangle^2 \right] \tag{39}$$

The procedure for obtaining the maximally localized orbitals is to introduce the transformation in Eq. (38) into Eq. (39) and then to minimize the spread functional with respect to U_{ij}:

$$\frac{\partial}{\partial U_{ij}} \Omega[\{\psi'\}] = 0 \tag{40}$$

The minimization must be carried out subject to the constraint the U_{ij} be an element of SU(N_s). This constraint condition can be eliminated if we choose U to have the form $\mathrm{U} = \exp(i\mathrm{A})$, where A is an $N_s \times N_s$ Hermitian matrix, and performing the minimization of Ω with respect to A.

A little reflection reveals that the spread functional in Eq. (39) is actually not suitable for periodic systems. The reason for this is that the position operator $\hat{\mathbf{r}}$ lacks the translational invariance of the underlying periodic supercell. A generalization of the spread functional that does not suffer from this deficiency is (Berghold et al., 2000; Resta & Sorella, 1999)

$$\Omega[\{\psi\}] = \frac{1}{(2\pi)^2} \sum_{i=1}^{N_s} \sum_I \omega_I f(|z_{I,ii}|^2) + \mathcal{O}((\sigma/L)^2) \tag{41}$$

where σ and L denote the typical spatial extent of a localized orbital and box length, respectively, and

$$z_{I,ii} = \int d\mathbf{r}\ \psi_i^*(\mathbf{r}) e^{i\mathbf{G}_I \cdot \mathbf{r}} \psi_j(\mathbf{r}) \equiv \langle \psi_i | \hat{O}^I | \psi_j \rangle \tag{42}$$

Here $G_I = 2\pi(\mathbf{h}^{-1})^T \hat{\mathbf{g}}_I$, where $\hat{\mathbf{g}}_I = (l_I, m_I, n_I)$ is the Ith Miller index and ω_I is a weight having dimensions of (length)^2. The function $f(|z|^2)$ is often taken to be $1 - |z|^2$, although several choices are possible. The orbitals that result from minimizing Eq. (41) are known as *Wannier orbitals* $|w_i\rangle$. If $z_{I,ii}$ is evaluated with respect to these orbitals, then the orbital centers, known as *Wannier centers*, can be computed according to

$$w_\alpha = -\sum_\beta \frac{h_{\alpha\beta}}{2\pi} \mathrm{Im} \ln z_{\beta,ii} \tag{43}$$

Wannier orbitals and their centers are useful in analyzing chemically reactive systems and will be employed in the present surface chemistry studies.

Like the KS energy, the fictitious CP dynamics is invariant with respect to gauge transformations of the form given in Eq. (38). They are not, however, invariant under time-dependent unitary transformations of the form

$$\psi_i'(\mathbf{r}, t) = \sum_{j=1}^{N_s} U_{ij}(t) \psi_j(\mathbf{r}, t) \tag{44}$$

and consequently, the orbital gauge changes at each step of an AIMD simulation. If, however, we impose the requirement of invariance under Eq. (44) on the CP dynamics, then not only would we obtain a gauge-invariant version of the AIMD algorithm, but we could also then fix a particular orbital gauge and have this gauge be preserved under the CP evolution. Using techniques for gauge field theory, it is possible to devise such a AIMD algorithm (Thomas et al., 2004). Introducing orbital momenta $|\pi_i\rangle$ conjugate to the orbital degrees of freedom, the gauge-invariant AIMD equations of motion have the basic structure

$$\begin{aligned} M_I\ddot{\mathbf{R}}_I &= -\nabla_I\left[\mathcal{E}[\{\psi\},\mathbf{R}]+U_{\mathrm{NN}}(\mathbf{R})\right] \\ |\dot{\psi}_i\rangle &= |\pi_i\rangle+\sum_j B_{ij}(t)|\psi_j\rangle \\ |\dot{\pi}_i\rangle &= -\frac{1}{\mu}\frac{\partial}{\partial\langle\psi_i|}\mathcal{E}[\{\psi\},\mathbf{R}]+\sum_j\lambda_{ij}|\psi_j\rangle+\sum_j B_{ij}(t)|\pi_j\rangle \end{aligned} \tag{45}$$

where

$$B_{ij}(t)=\sum_k U_{ki}\frac{d}{dt}U_{kj} \tag{46}$$

Here, the terms involving the matrix $B_{ij}(t)$ are gauge-fixing terms that preserve a desired orbital gauge. If we choose the unitary transformation $U_{ij}(t)$ to be the matrix that satisfies Eq. (40), then Eqs. (45) will propagate maximally localized orbitals (Iftimie et al., 2004). As was shown in Iftimie et al. (2004); Thomas et al. (2004), it is possible to evaluate the gauge-fixing terms in a way that does not require explicit minimization of the spread functional (Sharma et al., 2003). In this way, if the orbitals are initially localized, they remain localized throughout the trajectory.

While the Wannier orbitals and Wannier centers are useful concepts, it is also useful to have a measure of electron localization that does not depend on a specific orbital representation, as the latter does have some arbitrariness associated with it. An alternative measure of electron localization that involves only the electron density $n(\mathbf{r})$ and the so-called kinetic energy density

$$\tau(\mathbf{r})=\sum_{i=1}^{N_s}|f_i\nabla\psi_i(\mathbf{r})|^2 \tag{47}$$

was introduced by Becke and Edgecombe (1990). Defining the ratio $\chi(\mathbf{r})=D(\mathbf{r})/D_0(\mathbf{r})$, where

$$\begin{aligned} D(\mathbf{r}) &= \tau(\mathbf{r})-\frac{1}{4}\frac{|\nabla n(\mathbf{r})|^2}{n(\mathbf{r})} \\ D_0(\mathbf{r}) &= \frac{3}{4}\left(6\pi^2\right)^{2/3}n^{5/3}(\mathbf{r}) \end{aligned} \tag{48}$$

the function $f(\mathbf{r})=1/(1+\chi^2(\mathbf{r}))$ can be shown to lie in the interval $f(\mathbf{r})\in[0,1]$, where $f(\mathbf{r})=1$ corresponds to perfect localization, and $f(\mathbf{r})=1/2$ corresponds to a gas-like localization. The function $f(\mathbf{r})$ is known as the *electron localization function* or ELF. In the studies to be presented below, we will make use both of the ELF and the Wannier orbitals and centers to quantify electron localization.

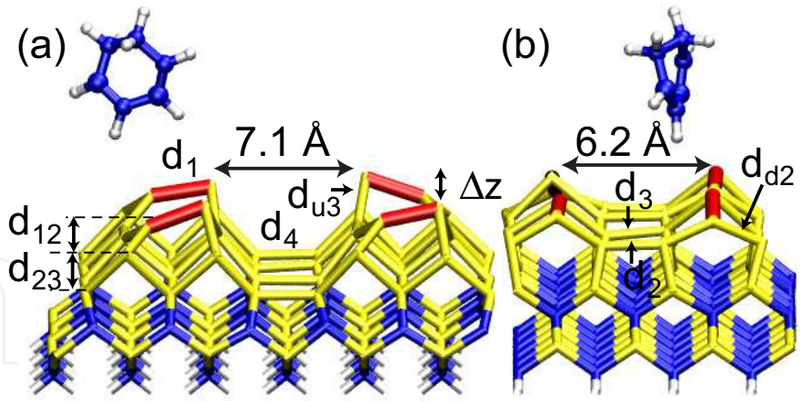

Fig. 1. View of 1,3-CHD + 3C-SiC(001)-3×2 system (a) along dimer rows and (b) between dimers in a row. Si, C, H, and the top Si surface dimers are represented by yellow, blue, white, and red, respectively. The dimers are spaced farther apart by ∼60% along a dimer row and ∼20% across dimer rows relative to Si(100)-2×1.

3. Reactions on the 3C-SiC(001)-3×2 surface

Silicon-carbide (SiC) and its associated reactions with a conjugated diene is an interesting surface to study and to compare to the pure silicon surface. In previous work (Hayes & Tuckerman, 2007; Minary & Tuckerman, 2004; 2005), we have shown that when a conjugated diene reacts with the Si(100)-2×1 surface, a relatively broad distribution of products results, in agreement with experiment (Teague & Boland, 2003; 2004), because the surface dimers are relatively closely spaced. Because of this, creating ordered organic layers on this surface using conjugated dienes seems unlikely unless some method can be found to enhance the population of one of the adducts, rendering the remaining adducts negligible. SiC exhibits a number of complicated surface reconstructions depending on the surface orientation and growth conditions. Some of these reconstructions offer the intriguing possibility of restricting the product distribution due to the fact that carbon-carbon or silicon-silicon dimer spacings are considerably larger.

SiC is often the material of choice for electronic and sensor applications under extreme conditions (Capano & Trew, 1997; Mélinon et al., 2007; Starke, 2004) or subject to biocompatibility constraints (Stutzmann et al., 2006). Although most reconstructions are still being debated both experimentally and theoretically (Pollmann & Krüger, 2004; Soukiassian & Enriquez, 2004), there is widespread agreement on the structure of the 3C-SiC(001)-3×2 surface (D'angelo et al., 2003; Tejeda et al., 2004)(see Fig. 1), which will be studied in this section. SiC(001) shares the same zinc blend structure as pure Si(001), but with alternating layers of Si and C. The top three layers are Si, the bottom in bulk-like positions and the top decomposed into an open 2/3 + 1/3 adlayer structure. Si atoms in the bottom two-thirds layers are 4-fold coordinated dimers while those Si atoms in the top one-third are asymmetric tilted dimers with dangling bonds. Given the Si-rich surface environment and presence of asymmetric surface dimers, one might expect much of the same Si-based chemistry to occur with two significant differences: (1) altered reactivity due to the surface strain (the SiC lattice constant is ∼ 20% smaller than Si) and (2) suppression of interdimer adducts due to the larger dimer spacing compared to Si (∼60% along a dimer row, ∼20% across dimer rows). Previous theoretical studies used either static (0 K) DFT calculations of hydrogen (Chang et al., 2005; Di Felice et al., 2005; Peng et al., 2007a; 2005; 2007b), a carbon

nanotube (de Brito Mota & de Castilho, 2006), or ethylene/acetylene (Wieferink et al., 2006; 2007) adsorbed on SiC(001)-3×2 or employed molecular dynamics of water (Cicero et al., 2004) or small molecules of the CH_3-X family (Cicero & Catellani, 2005) on the less thermodynamically stable SiC(001)-2×1 surface. Here, we consider cycloaddition reactions on the SiC-3×2 surface that include dynamic and thermal effects. A primary goal for considering this surface is to determine whether 3C-SiC(001)-3×2 is a promising candidate for creating ordered semiconducting-organic interfaces via cycloaddition reactions.

In the study Hayes and Tuckerman (2008), the KS orbitals were expanded in a plane-wave basis set up to a kinetic energy cut-off of 40 Ry. As in the 1,3-CHD studies described above, exchange and correlation are treated with the spin restricted form of the PBE functional (Perdew et al., 1996), and core electrons were replaced by Troullier-Martins pseudopotentials (Troullier & Martins, 1991) with S, P, and D treated as local for H, C, and Si, respectively. The resulting SiC theoretical lattice constant, 4.39 Å, agrees well with the experimental value of 4.36 Å (Tejeda et al., 2004). The full system is shown in Fig. 1. The 3×2 unit cell is doubled in both directions to include four surface dimers to allow the possibility of all interdimer adducts. Again, the resulting large surface area, (18.6 Å x 12.4 Å), allows the Γ-point approximation to be used in lieu of explicit k-point sampling. Two bulk layers of Si and C, terminated by H on the bottom surface, provide a reconstructed (1/3 + 2/3) Si surface in reasonable agreement with experiment (see below). The final system has 182 atoms [24 atoms/layer * (1 Si adlayer + 4 atomic layers) + 2*24 terminating H]. The simulation cell employed lengths of 18.6 Å and 12.4 Å along the periodic directions and 31.2 Å along the nonperiodic z direction.

Both the CHD and SiC(001) surface were equilibrated separately under NVT conditions using Nosé-Hoover chain thermostats (Martyna et al., 1992) at 300 K with a timestep of 0.1 fs for 1 ps and 3 ps, respectively. When the equilibrated CHD was allowed to react with the equilibrated surface, the time step was reduced to 0.05 fs in order to ensure adiabaticity. The CHD was placed 3 Å above the surface, as defined by the lowest point on the CHD and the highest point on the surface. Each of twelve trajectories was initiated from the same CHD and SiC structures but with the CHD placed at a different orientations and/or locations over the surface. The subsequent initialization procedure was identical to the CHD-Si(100) system: First the system was annealed from 0 K to 300 K in the NVE ensemble. Following this, it was equilibrated with Nosé-Hoover chain thermostats for 1 ps at 300K under NVT conditions, keeping the center of mass of the CHD fixed. Finally, the CHD center of mass constraint was removed and the system was allowed to evolve under the NVE ensemble until an adduct formed or 20 ps elapsed.

The reactions that occur on this surface all take place on or in the vicinity of a single surface Si-Si dimer. However, as Fig. 2 shows, there is not one but rather four adducts that are observed to form. Adduct labels from the Si + CHD study are used for consistency. As postulated, the widely spaced dimers successfully suppressed the interdimer adducts that formed on the Si(100)-2×1 surface (Hayes & Tuckerman, 2007). From the twelve trajectories, three formed the [4+2] Diels-Alder type intradimer adduct (A), one produced the [2+2] intradimer adduct (D), five exhibited hydrogen abstraction (H), and one resulted in a novel [4+2] subdimer adduct between Si in d_1 and d_2 (G) (see Fig. 1). The remaining trajectories only formed 1 C-Si bond within 20 ps. Although the statistics are limited, these results suggest that H abstraction is favorable, consistent with the high reactivity of atomic H observed in experimental studies on this system (Amy & Chabal, 2003; Derycke et al., 2003). What is somewhat more troublesome, from the point of view of creating well-ordered

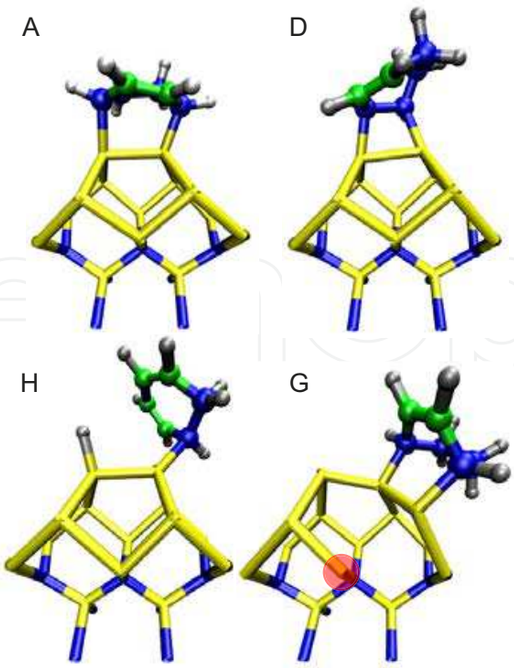

Fig. 2. Snapshots of the four adducts which formed on the SiC surface: (A) [4+2] intradimer adduct, (D) [2+2] intradimer adduct, (H) hydrogen abstraction, and (G) [4+2] subsurface dimer adduct. Si, C, and H are represented by yellow, blue, and silver, respectively. The remaining C=C bond(s) is highlighted in green. The larger spacing between dimers suppresses interdimer adducts. However, adduct (G) destroys the surface, rendering this system inappropriate for applications requiring well-defined organic-semiconducting interfaces.

organic-semiconducting interfaces is the presence of the subdimer adduct G. All the surface bonds directly connected to the adduct slightly expand to 2.42-2.47 Å, with the exception of one bond to a Si in the third layer, (highlighted in red in Fig. 2G) which disappears entirely. The energetic gain of the additional strong C-Si bond outweighs the loss of a strained Si-Si bond. The end effect is the destruction of the perfect surface and the creation of an unsaturated Si in the bulk. One adduct is noticeably missing: the [2+2] subdimer adduct. At several points during the simulation this adduct was poised to form but quickly left the vicinity. Most likely, the strain caused by the four-member ring combined with the two energetically less stable unsaturated Si prevented this adduct from forming, even though the [2+2] intradimer and [4+2] subdimer adducts are stable.

In Fig. 3, we show the carbon-carbon and CHD-Si distances as functions of time for the different adducts observed. This figure reveals that the mechanism of the reactions proceeds in a manner very similar to that of CHD and 1,3-butadiene on the Si(100)-2×1 surface: It is an asymmetric, nonconcerted mechanism that involves a carbocation intermediate. What differs from Si(100) is the time elapsed before the first bond forms and the intermediate lifetime. On the Si(100)-2×1 surface the CHD always found an available "down" Si to form the first bond within less than 10 ps or 40 Å of wandering over the surface. On the SiC(001)-3×2 surface the exploration process sometimes required up to 20 ps and over 100 Å. While the exact numbers are only qualitative, the trend is significant. The Si(100) dimers are more tilted on average, and hence expected to be slightly more reactive. However, the dominant contribution is

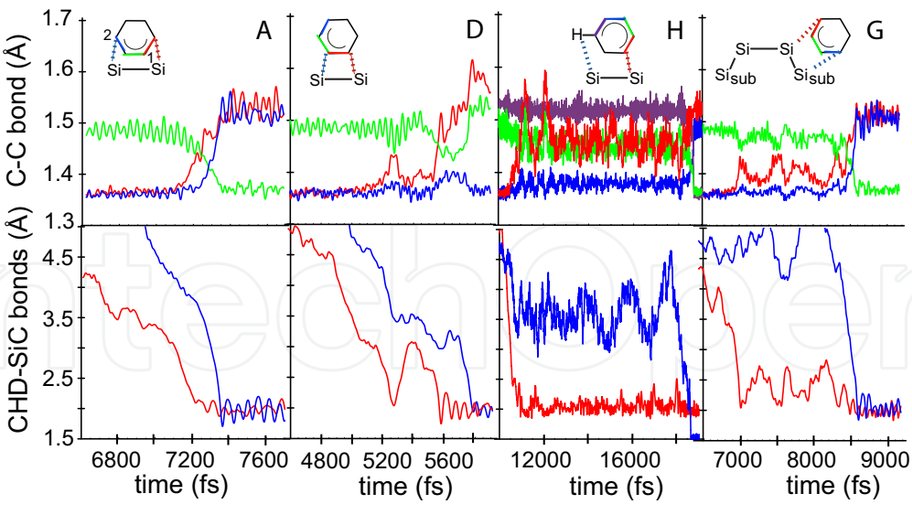

Fig. 3. Relevant bond lengths () vs time (fs) during product formation for four representative adducts. The top row displays the C-C bonds lengths (moving average over 25 fs) while the bottom row plots the first and second CHD - SiC surface bond. The color-coded inset identifies the bond being plotted for each adduct type. Change in the C-C bond length closely correlates with surface-adduct bond formation. Intermediate lifetimes over all trajectories range from 0.05 - 18^{+} ps.

likely the density of tilted dimers: Si has 0.033 dimers/Å^2, but SiC only has 0.017 dimers/Å^2. Regardless of whether dimer flipping occurs, it is simply more difficult to find a dimer on the SiC surface.

An important consideration in cycloaddition reactions such as those studied here is the possibility of their occurring through a radical mechanism. Multi-reference self consistent field cluster calculations of the SiC(001)-2x1 surface suggest that the topmost dimer exhibits significant diradical character (Tamura & Gordon, 2003), and since DFT is a single-reference method, multi-reference contributions are generally not included. However, cluster methods may bias the results by unphysically truncating the system instead of treating the full periodicity. For instance, cluster methods predict that Si(100)-2$\times$1 dimers are symmetric (Olson & Gordon, 2006), contrary to experimental evidence (Mizuno et al., 2004; Over et al., 1997), while periodic DFT correctly captures the dimer tilt (Hayes & Tuckerman, 2007). In order to estimate the importance of diradical mechanisms and surface crossing, a series of single point energy calculations at regular intervals during four representative trajectories are plotted in Fig. 4. Three electronic configurations are considered: singlet spin restricted (SR) where the up and down spin are identical (black down triangles), singlet spin unrestricted (SU) where the up and down spin can vary spatially (red up triangles), and triplet SU (green squares). In all cases, the triplet configuration is unfavorable. However, at two places in the transition state (Adduct A in Fig. 4a at 3000 fs and Adduct G in Fig. 4d at 8500 fs) the single SU is slightly favored. Thus, multi-reference methods, which can account for surface crossing, may yield alternative reaction mechanisms.

4. Reactions on the SiC(100)-2$\times$2 surface

There is considerable interest in the growth of molecular lines or wires on semiconductor surfaces. Such structures allow molecular scale devices to be constructed using

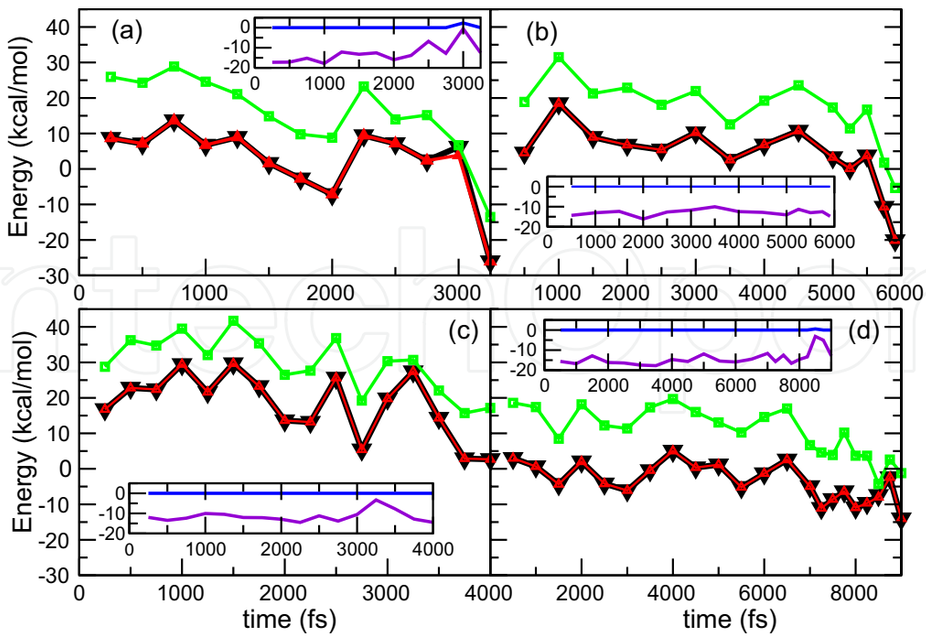

Fig. 4. Spin restricted (black down triangles), singlet spin-unrestricted (red up triangles), and triplet unrestricted (green squares) energies at regular intervals during a representative (a) [4+2] intradimer adduct [A], (b) [2+2] intradimer adduct [D], (c) H-abstraction, and (d) [4+2] subdimer trajectory. Energies are relative to the value at t=0 in (a). The insets show the difference between the spin restricted and unrestricted singlet energies (blue line) and spin restricted and triplet unrestricted energies (purple). The triplet configuration is always highest in energy. In (a) at 3000 fs and (d) at 8500 fs the singlet transition state configuration is favorable by 2.3 and 0.5 kcal/mol, respectively. Thus, a radical mechanism may also occur in this system.

semiconductors such as H-terminated Si(111) and Si(100) or Si(100)-2×1 as the preferred substrates. Various molecules can be grown into lines on the H-terminated surfaces (McNab & Polanyi, 2006), and on the Si(100)-2×1 surface, styrene and derivatives such as 2,4-dimethylstyrene or longer chain alkenes can be used to grow wires along the dimer rows (DiLabio et al., 2007; 2004; Hossain et al., 2005a;c; 2007a;b; 2008; Zikovsky et al., 2007). More recently, allylic mercaptan and acetophenone have been shown to grow across dimer rows on the H:Si(100)-2×1 surface (Ferguson et al., 2009; 2010; Hossain et al., 2005c; 2008; 2009). Other semiconductor surface can be considered for such applications, however, these have not received as much attention. An intriguing possible alternate in the silicon-carbide family is the SiC(100)-2×2 surface.

The SiC(100)-2×2 surface exhibits the crucial difference from the SiC(100)-3×2 in that it is characterized by C≡C triple bonds, which bridge Si-Si single bonds. These triple bonds are well separated and reactive, suggesting the possibility of restricting the product distribution for the addition of conjugated dienes on this surface. Fig. 5 shows a snapshot of this surface. Previous *ab initio* calculations suggest that these dimers react favorably with 1,4-cyclohexadiene (Bermudez, 2003). Here, we present new results on the free energy profile at 300 K for the reaction of this surface with 1,3-cyclohexadiene.

In general, reaction mechanisms and thermodynamic barriers for the cycloaddition reactions studied here can be analyzed by computing a free energy profile for one of the product states,

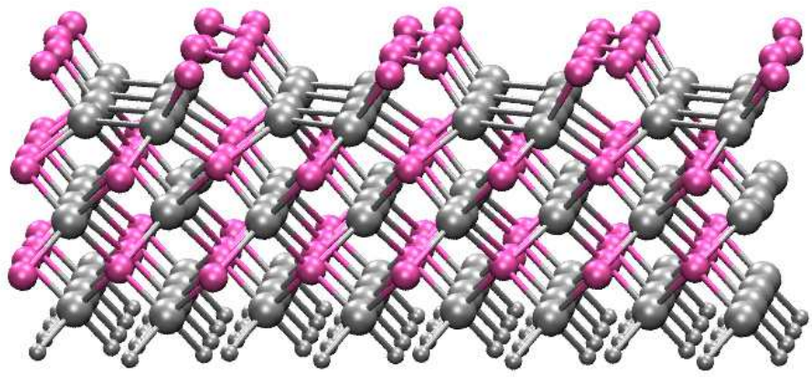

Fig. 5. Snapshot of the SiC-2×2 surface. Pink and grey spheres represent carbon and silicon atoms, respectively.

which we take to be the Diels-Alder-type [4+2] intradimer product. In the present case, the expect some of the barriers to product formation to be sufficiently high that specialized free energy sampling techniques are needed. Here, we employ the so-called blue moon ensemble approach (Carter et al., 1989; Sprik & Ciccotti, 1998) combined with thermodynamic integration. In order to define such a free energy profile, we first need to specify a reaction coordinate capable of following the progress of the reaction. For this purpose, we choose a coordinate ξ of the form

$$\xi = \frac{1}{2}\left|\left(\mathbf{r}_{C_a^s} + \mathbf{r}_{C_b^s}\right) - \left(\mathbf{r}_{C_1^m} + \mathbf{r}_{C_4^m}\right)\right| \tag{49}$$

where C_1^m and C_4^m are the carbons in the 1 and 4 positions in the organic molecule, and C_a^s and C_b^s are the two surface carbon atoms with which covalent bonds will form with C_1^m and C_4^m. Over the course of the reactions considered, ξ decreases from approximately 4 Å to a value less than 1.5 Å. In the aforementioned blue moon ensemble approach (Carter et al., 1989; Sprik & Ciccotti, 1998), the coordinate ξ is constrained at a set of equally spaced points between the two endpoints. At each constrained value, an AIMD simulation is performed over which we compute a conditional average $\langle \partial H/\partial \xi \rangle_{\text{cond}}$, where H is the nuclear Hamiltonian. Finally, the full free energy profile is reconstructed via thermodynamic integration:

$$\Delta G(\xi) = \int_{\xi_0}^{\xi} d\xi' \left\langle \frac{\partial H}{\partial \xi'} \right\rangle_{\text{cond}} \tag{50}$$

An example of such a free energy profile for the [4+2] cycloaddition reaction of 1,3-butadiene with a single silicon surface dimer on the Si(100)-2×1 surface is shown in Fig. 6 (Minary & Tuckerman, 2004). We show this profile as an example in order that direct comparison can be made between reactions on this surface and those on the SiC(100)2×2 surface. The profile in Fig. 6 shows an initial barrier at ξ =3.2 Åof approximately 23 kcal/mol. As ξ decreases, a shallow minimum/plateau is seen at ξ =2.75 Å, and such a minimum indicates a stable intermediate. This intermediate was identified as a carbocation in which one of the C-Si bonds had formed prior to the second bond formation (Hayes & Tuckerman, 2007; Minary & Tuckerman, 2004; 2005). This stable intermediate was interpreted as clear evidence that the reaction proceeds via an asymmetric, non-concerted mechanism.

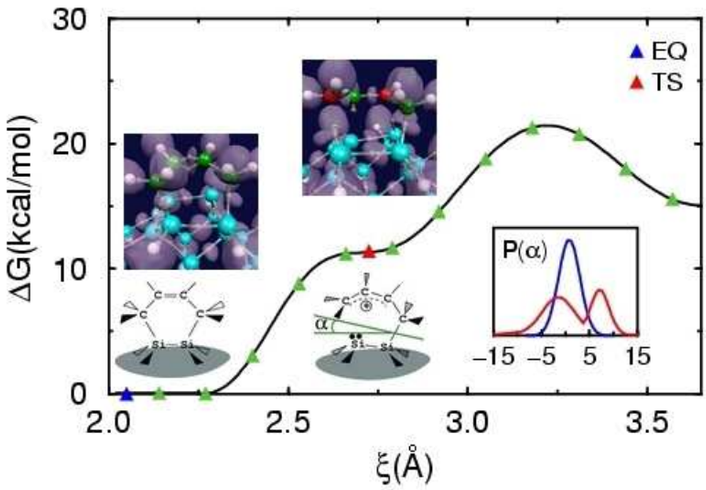

Fig. 6. Free energy along the reaction pathway leading to a Diels–Alder [4+2] adduct. Blue and red triangles indicate the product (EQ) and intermediate states (IS), respectively. Inset shows the buckling angle (α) distribution of the Si dimer for both the IS (red) and the EQ configurations (blue). The snapshots include configurations representing the IS and EQ geometries. Blue, green, and white spheres denote Si, C, and H atoms, respectively, and gray spheres indicate the location of Wannier centers. Red spheres locate positively charged atoms. The purple surface is a 0.95 electron localization function (ELF) isosurface.

In the present study of 1,3-cyclohexadiene with the SiC(100)-2×2 surface, the KS orbitals were expanded in a plane-wave basis set up to a kinetic energy cut-off of 60 Ry. As in the 1,3-CHD studies described above, exchange and correlation are treated with the spin restricted form of the PBE functional (Perdew et al., 1996), and core electrons were replaced by Troullier-Martins pseudopotentials (Troullier & Martins, 1991) with S, P, and D treated as local for H, C, and Si, respectively. The periodic slab contains 128 atoms arranged in 6 layers (including a bottom passivating hydrogen layer). Proper treatment of surface boundary conditions allowed for a simulation cell with dimensions L_x = 17.56Å, L_y =8.78 Å, and L_z =31 Å along the nonperiodic dimension. The surface contains 8 C≡C dimers. This setup is capable of reproducing the experimentally observed dimer buckling (Derycke et al., 2000) that static *ab initio* calculations using cluster models are unable to describe (Bermudez, 2003). In Fig. 7, we show the free energy profile for the [4+2] cycloaddition reaction of 1,3-cyclohexadiene with one of the C≡C surface dimers. The free energy profile is calculated by dividing the ξ interval $\xi \in [1.59, 3.69]$ into 15 equally spaced intervals, and each constrained simulation was equilibrated for 1.0 ps followed by 3.0 ps of averaging using a time step of 0.025 fs. All calculations are carried out in the NVT ensemble at 300 K using Nosé-Hoover chain thermostats (Martyna et al., 1992) In contrast to the free energy profile of Fig. 6, the profile in Fig. 7 shows no evidence of a stable intermediate. Rather, apart from an initial barrier of approximately 8 kcal/mol, the free energy is strictly downhill. The reaction is thermodynamically favored by approximately 48 kcal/mol. The suggestion from Fig. 7 is that the reaction is symmetric and concerted in contrast to the reactions on the other surfaces we have considered thus far. Fig. 7 shows snapshots of the molecule and the surface atoms

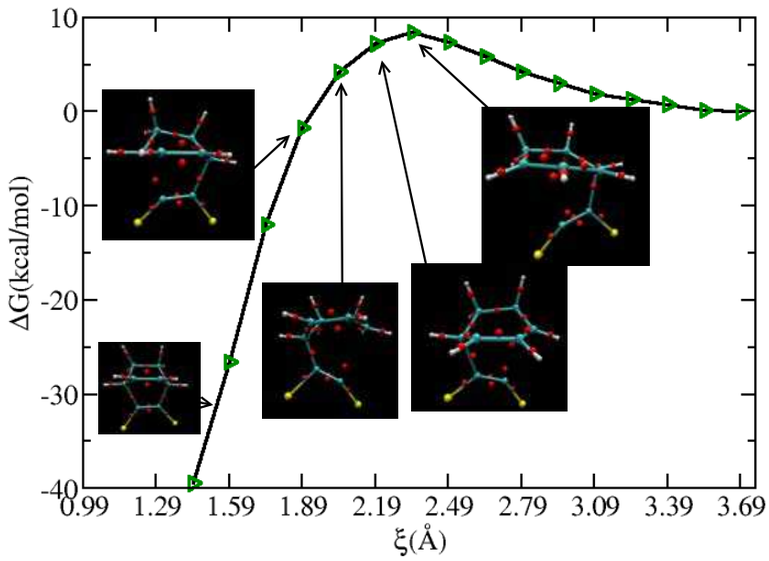

Fig. 7. Free energy profile for the formation of the [4+2] Diels-Alder-like adduct between 1,3-cyclohexadiene a C≡C dimer on the SiC-2×2 surface. Blue, white and yellow spheres represent C, H, and Si, respectively. Red spheres are the centers of maximally localized Wannier functions.

with which it interacts at various points along the free energy profile. In these snapshots, red spheres represent the centers of maximally localized Wannier functions. These provide a visual picture of where new covalent bonds are forming as the reaction coordinate ξ is decreased. By following these, we clearly see that one CC bond forms before the other, demonstrating the asymmetry of the reaction, which is a result of the buckling of the surface dimers. The buckling gives rise to a charge asymmetry in the C≡C surface dimer, and as a result, the first step in the reaction is a nucleophilic attack of one of the C=C bonds in the cyclohexadiene on the positively charged carbon in the surface dimer, this carbon being the lower of the two. Once this first CC bond forms, the second CC bond follows after a change of approximately 0.3 Å in the reaction coordinate with no stable intermediate along the way toward the final [4+2] cycloaddition product. In addition, the Wannier centers show the conversion of the triple bond on the surface to a double bond in the final product state.
Further evidence for the concerted asymmetric nature of the reaction is provided in Fig. 8, which shows the average carbon-carbon lengths computed over the constrained trajectories at each point of the free energy profile. It can be seen by the fact that one CC bond forms before the other that there is a slight tendency for an asymmetric reaction, despite its being concerted.
In order to demonstrate that the [4+2] Diels-Alder type cycloaddition product is highly favored over other reaction products on this surface, we show one additional example of a free energy profile, specifically, that for the formation of a [2+2] cycloaddition reaction with a single surface C≡C dimer. This profile is shown in Fig. 9. In contrast to the [4+2] Diels-Alder type adduct, the barrier to formation of this adduct is roughly 27 kcal/mol (compared to 8 kcal/mol for the Diels-Alder product). Thus, although the [2+2] reaction

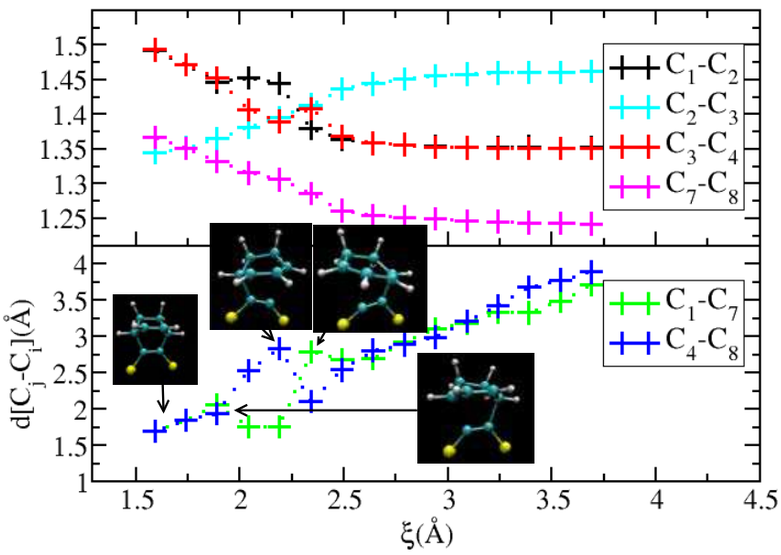

Fig. 8. Average carbon-carbon bond lengths obtained from each constrained simulation.

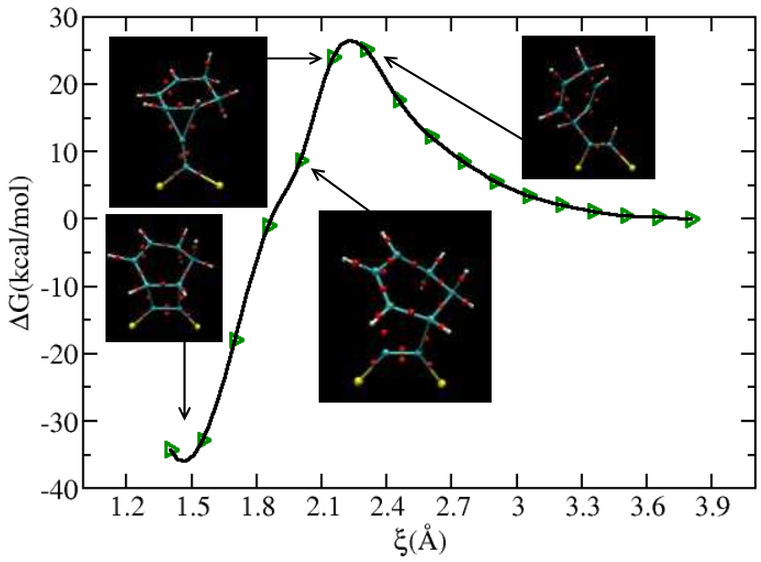

Fig. 9. Free energy profile for the formation of the [2+2] adduct between 1,3-cyclohexadiene a C≡C dimer on the SiC-2×2 surface. Blue, white and yellow spheres represent C, H, and Si, respectively. Red spheres are the centers of maximally localized Wannier functions.

is thermodynamically favorable, this barrier is sufficiently high that we would expect this particular reaction channel to be highly suppressed compared to one with a 19 kcal/mol lower barrier. The free energy profile, together with the snapshots taken along the reaction path, also suggests that this reaction occurs via an asymmetric, concerted mechanism, as was found for the [4+2] Diels-Alder type product.

Although we have not shown them here, we have computed free energy profiles for a variety of other adducts, including interdimer and sublayer adducts, and in all cases, free energy barriers exceeding 20 kcal/mol (or 40 kcal/mol in the case of the sublayer adduct) were obtained. These results strongly suggest that the product distribution this surface would, for all intents and purposes, restricted to the single [4+2] Diels-Alder type product, implying that this surface might be a candidate for creating an ordered organic/semiconductor interface.

5. References

Amy, F. & Chabal, Y. J. (2003). Interaction of H, O_2, and H_2O with 3C-SiC surfaces, *J. Chem. Phys.* 119: 6201–6209.

Basu, R., Kinser, C. R., Tovar, J. D. & Hersam, M. C. (2006). Bromine functionalized molecular adlayers on hydrogen passivated silicon surfaces, *Chem. Phys.* 326: 144–150.

Becke, A. D. (1988). Density-functional exchange-energy approximation with correct asymptotic behavior, *Phys. Rev. A* 38: 3098–3100.

Becke, A. D. & Edgecombe, K. E. (1990). A simple measure of electron localization in atomic and molecular systems, *J. Chem. Phys.* 92: 5397.

Berghold, G., Mundy, C. J., Romero, A. H., Hutter, J. & Parrinello, M. (2000). General and efficient algorithms for obtaining maximally localized wannier functions, *Phys. Rev. B* 61: 10040–10048.

Bermudez, V. M. (2003). Computational study of cycloaddition reactions on the SiC(100)-c(2x2) surface, *Surf. Sci.* 540(2–3): 255–264.

Capano, R. J. & Trew, R. J. (1997). Silicon carbide electronic devices and materials, *MRS Bulletin* 22: 19.

Car, R. & Parrinello, M. (1985). Unified approach for molecular dynamics and density-functional theory, *Phys. Rev. Lett.* 55: 2471–2474.

Carter, E. A., Ciccotti, G., Hynes, J. T. & Kapral, R. (1989). Constrained reaction coordinate dynamics for the simulation of rare events, *Chem. Phys. Lett.* 156: 472.

Cattaruzza, F., Cricenti, A., Flamini, A., Girasole, M., Longo, G., Prosperi, T., Andreano, G., Cellai, L. & Chirivino, E. (2006). Controlled loading of oligodeoxyribonucleotide monolayers onto unoxidized crystalline silicon; fluorescence-based determination of the surface coverage and of the hybridization efficiency; parallel imaging of the process by atomic force microscopy, *Nucl. Acids Res.* 34: e32.

Chang, H., Wu, J., Gu, B.-L., Liu, F. & Duan, W. (2005). Physical origin of hydrogen-adsorption-induced metallization of the SiC surface: *n*-type doping via formation of hydrogen bridge bond, *Phys. Rev. Lett.* 95: 196803.

Cicero, G. & Catellani, A. (2005). Towards sic surface functionalization: An *ab initio* study, *J. Chem. Phys.* 122: 214716.

Cicero, G., Catellani, A. & Galli, G. (2004). Atomic control of water interaction with biocompatible surfaces: The case of SiC(001), *Phys. Rev. Lett.* 93(1): 016102.

D'angelo, M., Enriquez, H., Aristov, V. Y., Soukiassian, P., Renaud, G., Barbier, A., Noblet, M., Chiang, S. & Semond, F. (2003). Atomic structure determination of the

Si-rich β-SiC(001)-3$\times$2 surface by grazing-incidence x-ray diffraction: A stress-driven reconstruction, *Phys. Rev. B* 68: 165321.

de Brito Mota, F. & de Castilho, C. M. C. (2006). Carbon nanotube adsorbed on a hydrogenated Si-rich β- SiC(100)(3$\times$2) surface: First principles pseudopotential calculations, *Phys. Rev. B* 74: 165408.

Derycke, V., Soukiassian, P. G., Amy, F., Chabal, Y., D'Angelo, M. D., Enriquez, H. B. & Silly, M. G. (2003). Nanochemistry at the atomic scale revealed in hydrogen-induced semiconductor surface metallization, *Nat. Mater.* 2: 253–254.

Derycke, V., Soukiassian, P., Mayne, A. & Dujardin, G. (2000). Scanning tunneling microscopy investigation of the C-terminated β-SiC(100) c(2$\times$2) surface reconstruction: Dimer orientation, defects, and antiphase boundaries, *Surf. Sci.* 446: L101–L107.

Di Felice, R., Bertoni, C. M., Pignedoli, C. A. & Catellani, A. (2005). Hydrogen-Induced Surface Metallization of β-SiC(001)-(3$\times$2) Revisted by Density Functional Theory Calculations, *Phys. Rev. Lett.* 94: 116103.

DiLabio, G. A., Dogel, S. A., Anagaw, A., Pitters, J. L. & Wolkow, R. A. (2007). Theoretical and spectroscopic study of the reaction of diethylhydroxylamine on silicon(100)-2 x 1, *Phys. Chem. Chem. Phys.* 9: 1629.

DiLabio, G. A., Piva, P. G., Kruse, P. & Wolkow, R. A. (2004). Dispersion interactions enable the self-directed growth of linear alkane nanostructures covalently bound to silicon, *J. Am. Chem. Soc.* 126: 16048.

Ferguson, G. A., Than, C. T. L. & Raghavachari, K. (2009). Line growth on the h/si(100)-2 x 1 surface: Density functional study of allylic mercaptan reaction mechanisms, *J. Phys. Chem. C* 113: 11817.

Ferguson, G. A., Than, C. T. L. & Raghavachari, K. (2010). Extending molecular lines on the si(100)-2 x 1 surface: A theoretical study of the effect of allylic mercaptan adsorbates on radical chain reactions, *J. Phys. Chem. C* 1: 679.

Filler, M. A. & Bent, S. F. (2002). The surface as molecular reagent: Organic chemistry at the semiconductor interface, *Prog. Surf. Sci.* 73: 1–56.

Filler, M. A. & Bent, S. F. (2003). The surface as molecular reagent: organic chemistry at the semiconductor interface, *Prog. Surf. Sci.* 73: 1–56.

Flatt, A., Chen, B. & Tour, J. (2005). Fabrication of carbon nanotube-molecule-silicon junctions, *J. Am. Chem. Soc.* 127: 8918.

Guisinger, N., Basu, R., Greene, M., Baluch, A. & Hersam, M. (2004). Observed suppression of room temperature negative differential resistance in organic monolayers on si(100), *Nanotechnology* 15: S452.

Guisinger, N., Greene, M., Basu, R., Baluch, A. & Hersam, M. (2004). Room temperature negative differential resistance through individual organic molecules on silicon surfaces, *Nano. Lett.* 4: 55.

Hayes, R. L. & Tuckerman, M. E. (2007). Role of surface dimer dynamics in the creating ordered organic-semiconductor interfaces, *J. Am. Chem. Soc.* 129: 12172–12180.

Hayes, R. L. & Tuckerman, M. E. (2008). Kinetic effects on the cycloaddition of 1,3-cyclohexadiene to the 3c-sic(001)-3x2 surface studied via ab initio molecular dynamics, *J. Phys. Chem. C* 112: 5880–5887.

He, J., Chen, B., Flatt, A., Stephenson, J., Condell, D. & Tour, J. (2006). Metal-free silicon-molecule-nanotube testbed and memory device, *Nature Materials* 5: 63.

Hohenberg, P. & Kohn, W. (1964). Inhomogeneous electron gas, *Phys. Rev. B* 136: 864–871.

Hossain, M. Z., Kato, H. S. & Kawai, M. (2005a). Controlled fabrication of 1d molecular lines across the dimer rows on the si(100)-(2x1)-h surface through the radical chain reaction, *J. Am. Chem. Soc.* 127: 15030.

Hossain, M. Z., Kato, H. S. & Kawai, M. (2005b). Controlled fabrication of 1d molecular lines across the dimer rows on the si(100)-2x1-h surface throught the radical chain reaction, *J. Am. Chem. Soc.* 127: 15030–15031.

Hossain, M. Z., Kato, H. S. & Kawai, M. (2005c). Fabrication of interconnected 1d molecular lines along and across the dimer rows on the si(100)-(2 x 1)-h surface through the radical chain reaction, *J. Phys. Chem. B* 109: 23129.

Hossain, M. Z., Kato, H. S. & Kawai, M. (2007a). Competing forward and reversed chain reactions in one-dimensional molecular line growth on the si(100)-(2 x 1)-h surface, *J. Am. Chem. Soc.* 129: 3328.

Hossain, M. Z., Kato, H. S. & Kawai, M. (2007b). Selective chain reaction of acetone leading to the successive growth of mutually perpendicular molecular lines on the si(100)-(2x1)-h surface, *J. Am. Chem. Soc.* 129: 12304.

Hossain, M. Z., Kato, H. S. & Kawai, M. (2008). Self-directed chain reaction by small ketones with the dangling bond site on the si(100)-(2 x 1)-h surface: Acetophenone, a unique example, *J. Am. Chem. Soc.* 130: 11518.

Hossain, M. Z., Kato, H. S. & Kawai, M. (2009). Valence states of one-dimensional molecular assembly formed by ketone molecules on the si(100)-(2 x 1)-h surface, *J. Phys. Chem. C* 113: 10751.

Iftimie, R., Thomas, J. W. & Tuckerman, M. E. (2004). On-the-fly localization of electronic orbitals in car-parrinello molecular dynamics, *J. Chem. Phys.* 120: 2169.

Kachian, J. S., Wong, K. T. & Bent, S. F. (2010). Periodic trends in organic functionalization of group iv semiconductor surfaces, *Acc. Chem. Res.* 43: 346–355.

Kirczenow, G., Piva, P. G. & Wolkow, R. A. (2005). Linear chains of styrene and methylstyrene molecules and their heterojunctions on silicon: Theory and experiment, *Phys. Rev. B* 72: 245306.

Kohn, W. & Sham, L. J. (1965). Self-consistent equations including exchange and correlation effects, *Phys. Rev. A* 140: 1133–1138.

Kruse, P. & Wolkow, R. A. (2002). Gentle lithography with benzene on si(100), *Appl. Phys. Lett.* 81: 4422.

Lee, C., Yang, W. & Parr, R. G. (1988). Development of the colle-salvetti correlation-exchange formula into a functional of the electron density, *Phys. Rev. B* 37: 785–789.

Lopinski, G. P., Wayner, D. D. M. & Wolkow, R. A. (2000). Self directed growth of molecular nanostructures on silicon, *Nature* 406: 48–51.

Martyna, G. J., Klein, M. L. & Tuckerman, M. E. (1992). Nose-Hoover Chains - the canonical ensemble via continuous dynamics, *J. Chem. Phys.* 97: 2635–2643.

Marx, D. & Hutter, J. (2000). *Modern Methods and Algorithms of Quantum Chemistry*, NIC, FZ Juelich, chapter Ab Initio Molecular Dynamics: Theory and Implementations, pp. 301–449.

Marx, D. & Hutter, J. (2009). *Ab Initio Molecular Dynamics*, Cambridge University Press, Cambridge.

Marx, D., Tuckerman, M. & Martyna, G. (1999). Quantum dynamics via adiabatic ab initio centroid molecular dynamics, *Comp. Phys. Comm.* 118: 166–184.

McNab, I. R. & Polanyi, J. C. (2006). Molecules on h-terminated si(111), *Chem. Rev.* 106: 4321.

Mélinon, P., Masenelli, B., Tournus, F. & Perez, A. (2007). Playing with carbon and silicon at the nanoscale, *Nat. Mater.* 6: 479–490.

Minary, P., Morrone, J. A., Yarne, D. A., Tuckerman, M. E. & Martyna, G. J. (2004). Long range interactions on wires: A reciprocal space based formalism, *J. Chem. Phys.* 121: 11949–11956.

Minary, P. & Tuckerman, M. E. (2004). Reaction pathway of the [4+2] diels-alder adduct formation on si(100)-2x1, *J. Am. Chem. Soc.* 126: 13920–13921.

Minary, P. & Tuckerman, M. E. (2005). Reaction mechanism of cis-1,3-butadiene addition to the si(100)-2x1 surface, *J. Am. Chem. Soc.* 127: 1110–1111.

Minary, P., Tuckerman, M. E., Pihakari, K. A. & Martyna, G. J. (2002). A new reciprocal space based treatment of long range interactions on surfaces, *J. Chem. Phys.* 116: 5351–5362.

Mizuno, S., Shirasawa, T., Shiraishi, Y. & Tochihara, H. (2004). Structure determination of Si(100)-c(4x2) surfaces at 80 K and electron beam effect below 40 K studied by low-energy electron diffraction, *Phys. Rev. B* 69: 241306.

Olson, R. M. & Gordon, M. S. (2006). The structure of the Si_9H_{12} cluster: A coupled cluster and multi-reference perturbation theory study, *J. Chem. Phys.* 124: 081105.

Over, H., Wasserfall, J., Ranke, W., Ambiatello, C., Sawitzki, R., Wolf, D. & Moritz, W. (1997). Surface atomic geometry of Si(001)-(2x1): A low-energy electron-diffraction structure analysis, *Phys. Rev. B* 55: 4731–4736.

Peng, X., Krüger, P. & Pollmann (2007a). Hydrogenated sic(001)-(3x2) surface: Semiconducting and metallic structures, *Phys. Rev. B* 76: 125303.

Peng, X., Krüger, P. & Pollmann, J. (2005). Metallization of the 3C-SiC(001)-(3x2) surface induced by hydrogen adsorption: A first-principles investigation, *Phys. Rev. B* 72: 245320.

Peng, X., Krüger, P. & Pollmann, J. (2007b). Why thermal h_2 molecules adsorb on sic(001)-c(4x2) and not on sic(001)-(3x2) at room temperature, *Phys. Rev. B* 75: 073409.

Perdew, J. P., Burke, K. & Ernzerhof, M. (1996). Generalized gradient approximation made simple, *Phys. Rev. Lett.* 77: 3865–3868.

Pitters, J. L., Dogel, I., DiLabio, G. A. & Wolkow, R. A. (2006). Linear nanostructure formation of aldehydes by self-directed growth on hydrogen-terminated silicon(100), *J. Phys. Chem. B* 110: 2159–2163.

Pollmann, J. & Krüger, P. (2004). Reconstruction models of cubic SiC surfaces, *J. Phys.-Condens. Mat.* 16: S1659–S1703.

Rakshit, T., Liang, G., Ghosh, A. & Datta, S. (2004). Silicon-based molecular electronics, *Nano lett.* 4: 1803.

Resta, R. & Sorella, S. (1999). Electron localization in the insulating state, *Phys. Rev. Lett.* 82: 370–373.

Sharma, M., Wu, Y. D. & Car, R. (2003). Ab initio molecular dynamics with maximally localized wannier functions, *Intl. J. Quant. Chem.* 95: 821.

Soukiassian, P. G. & Enriquez, H. B. (2004). Atomic scale control and understanding of cubic silicon carbide surface reconstructions, nanostructures and nanochemistry, *J. Phys.-Condens. Mat.* 16: S1611–S1658.

Sprik, M. & Ciccotti, G. (1998). Free energy from constrained molecular dynamics, *J. Chem. Phys.* 109: 7737.

Starke, U. (2004). *Silicon Carbide: Fundamental Questions and Applications to current device technology*, Springer-Verlag, Berlin, Germany.

Stutzmann, M., Garrido, J. A., Eickhoff, M. & Brandt, M. S. (2006). Direct biofunctionalization of semiconductors: A survey, *Phys. Stat. Sol. A* 203(14): 3424–3437.

Tamura, H. & Gordon, M. S. (2003). Multiconfigurational self-consistent field study of the silicon carbide (001) surface, *J. Chem. Phys.* 119: 10318–10324.

Teague, L. C. & Boland, J. J. (2003). Stm study of multiple bonding configurations and mechanism of 1,3-cyclohexadiene attachment on si(100)-2x1, *J. Phys. Chem. B* 107: 3820–3823.

Teague, L. C. & Boland, J. J. (2004). Kinetically controlled reaction of 1,3-cyclohexadiene on si(100), *Thin Solid Films* 464-465: 1–4.

Tejeda, A., Dunham, D., García de Abajo, F. J., Denlinger, J. D., Rotenberg, E., Michel, E. G. & Soukiassian, P. (2004). Photoelectron diffraction study of the si-rich 3c-sic(001)-(3x2) structure, *Phys. Rev. B* 70: 045317.

Thomas, J. W., Iftimie, R. & Tuckerman, M. E. (2004). Field theoretic approach to dynamical orbital localization in ab initio molecular dynamics, *Phys. Rev. B* 69: 125105.

Troullier, N. & Martins, J. L. (1991). Efficient pseudopotentials for plane-wave calculations, *Phys. Rev. B* 43: 1993–2006.

Tuckerman, M. E. (2002). *Ab initio* molecular dynamics: Basic concepts, current trends and novel applications, *J. Phys.-Condens. Mat.* 14: R1297–R1355.

Tuckerman, M. E. & Martyna, G. J. (1999). A reciprocal space based method for treating long range interactions in ab initio and force-field-based calculations in clusters, *J. Chem. Phys.* 110: 2810–2821.

Tuckerman, M. E. & Parrinello, M. (1994). Integrating the car-parrinello equations .1. basic integration techniquesunified approach for molecular dynamics and density-functional theory, *J. Chem. Phys.* 101: 1302–1315.

Tuckerman, M. E., Yarne, D. A., Samuelson, S. O., Hughes, A. L. & Martyna, G. J. (2000). Exploiting multiple levels of parallelism in molecular dynamics based calculations via modern techniques and software paradigms on distributed memory computers, *Comput. Phys. Commun.* 128: 333–376.

Wieferink, J., Krüger, P. & Pollmann, J. (2006). Improved hybrid algorithm with Gaussian basis sets and plane waves: First-principles calculations of ethylene adsorption on β-SiC(001)-(3$\times$2), *Phys. Rev. B* 74: 205311.

Wieferink, J., Krüger, P. & Pollmann, J. (2007). First-principles study of acetylene adsorption on β-SiC(001)-(3$\times$2), *Phys. Rev. B* 75: 153305.

Zikovsky, J., Dogel, S. A., Haider, A. B., DiLabio, G. A. & Wolkow, R. A. (2007). Self-directed growth of contiguous perpendicular molecular lines on h-si(100) surfaces, *J. Phys. Chem. A* 111: 12257.

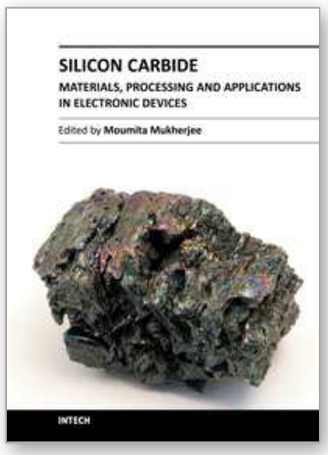

Silicon Carbide - Materials, Processing and Applications in Electronic Devices

Edited by Dr. Moumita Mukherjee

ISBN 978-953-307-968-4
Hard cover, 546 pages
Publisher InTech
Published online 10, October, 2011
Published in print edition October, 2011

Silicon Carbide (SiC) and its polytypes, used primarily for grinding and high temperature ceramics, have been a part of human civilization for a long time. The inherent ability of SiC devices to operate with higher efficiency and lower environmental footprint than silicon-based devices at high temperatures and under high voltages pushes SiC on the verge of becoming the material of choice for high power electronics and optoelectronics. What is more important, SiC is emerging to become a template for graphene fabrication, and a material for the next generation of sub-32nm semiconductor devices. It is thus increasingly clear that SiC electronic systems will dominate the new energy and transport technologies of the 21st century. In 21 chapters of the book, special emphasis has been placed on the â€œmaterialsâ€ aspects and developments thereof. To that end, about 70% of the book addresses the theory, crystal growth, defects, surface and interface properties, characterization, and processing issues pertaining to SiC. The remaining 30% of the book covers the electronic device aspects of this material. Overall, this book will be valuable as a reference for SiC researchers for a few years to come. This book prestigiously covers our current understanding of SiC as a semiconductor material in electronics. The primary target for the book includes students, researchers, material and chemical engineers, semiconductor manufacturers and professionals who are interested in silicon carbide and its continuing progression.

InTech Europe
University Campus STeP Ri
Slavka Krautzeka 83/A
51000 Rijeka, Croatia

InTech China
Unit 405, Office Block, Hotel Equatorial Shanghai
No.65, Yan An Road (West), Shanghai, 200040, China
中国上海市延安西路65号上海国际贵都大饭店办公楼405单元

Phone: +385 (51) 770 447
Fax: +385 (51) 686 166
www.intechopen.com

Phone: +86-21-62489820
Fax: +86-21-62489821

IntechOpen

IntechOpen